Templated Nanofiber Synthesis via Chemical Vapor Polymerization into Liquid Crystalline Films

Kenneth C. K. Cheng[1, 2, †], Marco A. Bedolla-Pantoja[3, †], Young-Ki Kim[3,6 †], Jason V. Gregory[1, 4], Fan Xie[1,4], Alexander de France[1,4], Christoph Hussal[5], Kai Sun[2], Nicholas L. Abbott[3,6]*, Joerg Lahann[1, 2, 4, 5,]*

Affiliations:

[1]Biointerfaces Institute, University of Michigan, Ann Arbor, Michigan, United States.

[2]Department of Materials Science and Engineering, University of Michigan, Ann Arbor, Michigan, United States.

[3]Department of Chemical and Biological Engineering, University of Wisconsin-Madison, Madison, Wisconsin, United States.

[4]Department of Chemical Engineering, University of Michigan, Ann Arbor, Michigan, United States.

[5]Institute of Functional Interfaces, Karlsruhe Institute of Technology, Karlsruhe, Germany.

[6]Department of Chemical and Biomolecular Engineering, Cornell University, Ithaca, New York, United States

[†]These authors contributed equally to this work.

*Corresponding author. Email: nabbott@cornell.edu (N.L.A.); lahann@umich.edu (J.L.)

Abstract: Extrusion, electrospinning and microdrawing are widely used to create fibrous polymer mats, but these approaches offer limited access to oriented arrays of nanometer-scale fibers with controlled size, shape and lateral organization. We show that chemical vapor polymerization can be performed on surfaces coated with thin films of liquid crystals to synthesize organized assemblies of end-attached polymer nanofibers. The process uses low concentrations of radical monomers formed initially in the vapor phase and then diffused into the liquid crystal template. This minimizes monomer-induced changes to the liquid crystal phase and enables access to nanofiber arrays with complex, yet precisely defined structures and compositions. The nanofiber arrays permit tailoring of a wide range of functional properties, including adhesion that depends on nanofiber chirality.

One Sentence Summary: The synthesis of organized arrays of end-attached polymeric nanofibers with precise diameter, lengths and shapes is reported.

Main Text:

Surfaces decorated with oriented arrays of fibers are ubiquitous in the natural world because they can provide functions such as sensing (hair cells (*1*)), thermal insulation (polar bear fur (*2*)), enhanced mass transport (microtubules (*3*)), extreme wetting properties (lotus leaf (*4*)), and reversible adhesion (gecko foot (*5*)). However, recreation of these functions in synthetic materials requires multiscale engineering of the composition, shape and morphology of individual fibers as well as control of higher order organization of fibers into arrays. We address this challenge by building from studies reported in 1916 by T. Svedberg (*6*) who used the long-range molecular order and fluidity inherent to liquid crystals (LCs) to control chemical reactions, principles that have since been exploited in a wide range of transformations based on unimolecular reactions (*7*), molecular self-assembly (*8*) or polymerizations (*9, 10*). A key limitation of LC-templated polymerization, however, has been perturbation of the LC phase by monomers that are dissolved into the LC prior to the polymerization and then consumed during polymerization (*9, 10*).

Chemical vapor polymerization (CVP) is a versatile process that employs a range of polymerization modes (Fig. 1A), including reaction pathways using [2.2]paracyclophanes (*11-13*) (Gorham process) or halogenated xylene precursors (Gilch process) (*14, 15*) and free radical ring-opening co-polymerization (ROP) using 5,6-benzo-2-methylene-1,3-dioxepane and [2.2]paracyclophanes (*16*). CVP is widely used for fabrication of consumer products (e.g., electronics and packaging) because it enables rapid and inexpensive conformal coating of large surface areas with polymer films (*12*). Whereas past studies used CVP to form continuous polymeric films on surfaces (*11-16*), we found that CVP of compound **1a** into micrometer-thick supported films of nematic LCs (Fig. 1, B and C) resulted in the formation of surfaces decorated with aligned arrays of nanofibers (Fig. 1, D and E). When nematic 4′-pentyl-4-biphenylcarbonitrile (5CB) was anchored on a silane-functionalized glass surface in a perpendicular orientation (i.e., homeotropic anchoring, Fig. 1D), the nanofibers were straight and aligned perpendicular to the surface. Removal of the LC (confirmed by Fourier-transform infrared spectroscopy (FTIR) and solid-state ^{13}C nuclear magnetic resonance (NMR) spectroscopy, figs. S1 and S2) revealed that the nanofibers were made of insoluble polymer, were anchored at one end to the surface, and were structurally amorphous (fig. S3) yet optically birefringent as confirmed by cross-polarized light microscopy (Fig. 1F). Insertion of a quarter wave plate between crossed-polarizers (Fig. 1, G and H) revealed that the refractive index was greatest along the fiber

axis, consistent with electron diffraction patterns (fig. S3B) indicating alignment of polymer chains along the main axis of the nanofibers (Fig. 1I) (*17*).

CVP into films that lacked fluidity (crystalline solid 5CB, Fig. 2A) or long-range order (isotropic liquid 5CB, Fig. 2C or silicone oil, Fig. 2D) did not yield nanofibers, indicating that long-range order and fluidity are both necessary requirements for the shape-controlled synthesis of nanofiber arrays (Fig. 2B). Replacement of 5CB with nematic E7 (a mixture of cyanobiphenyls, Fig. 1B), TL205 (a mixture of halogenated molecules, Fig. 1C) or other nematic LCs (fig. S4) yielded organized assemblies of nanofibers with well-defined yet distinct diameters: $D = 142 \pm 11$ nm in 5CB, 85 ± 9 nm in E7, and 69 ± 7 nm in TL205 (Fig. 2E). We hypothesized that the nanofiber diameter is controlled by the extrapolation length ξ, which is defined as K/W, where K is the average Frank elastic constant for splay and bend of the LC and W is the surface anchoring energy density. If an inclusion (here: nanofiber) in a LC grows to a size that exceeds ξ, the orientation-dependent interfacial energy associated with interaction of the LC with the surface of the inclusion (WD^2, where D is the inclusion size) exceeds the energetic cost of elastic deformation of the LC (KD), and the LC will elastically deform around the inclusion (*18, 19*). We tested the hypothesis that $D \approx K/W$ by using literature values of K at $T = 25$ °C (*18, 20*) and our experimental values of D to calculate W (Fig. 2E). Calculated values of W were ~10^{-4} J/m^2 (*21*) with $W_{TL205} > W_{E7} > W_{5CB}$, a ranking that is consistent with (i) the theoretical prediction that $W \propto (T_{NI} - T)^{2\beta}$ where $\beta = 0.4\text{-}0.5$ (*22, 23*) and T_{NI} is the nematic-isotropic phase transition temperature (T_{NI}) of the LCs (Fig. 2E) and (ii) independent experiments of the relative values of W of these LCs (fig. S5). We also found the average diameters of the nanofibers to depend on the temperature (T_{LC}) of the LC during CVP. For example, D increased with T (Fig. 2E and fig. S6), as theoretically predicted by $\xi = K/W \propto (T_{NI} - T)^{-\beta}$ (*22, 23*). Overall, these results are consistent with a mechanism of growth in which the elastic energy of the LC defines the nanofiber diameter (via ξ) and promotes preferential growth of the nanofibers along the alignment direction of the LCs.

We performed CVP of **1a** using homeotropically-oriented E7 films with thicknesses ranging from 5 to 22 μm and found that the lengths of the fibers closely matched the LC film thicknesses (Fig. 2F). The result confirms growth of the nanofibers along the LC (figs. S7 and S8). We also found that monomers with a wide range of chemical functional groups could be polymerized in LCs by CVP (Gorham process), yielding (i) ethynyl-functionalized nanofibers for click-based reactions with azide derivatives (**2b**, Fig. 2G), (ii) nanofibers that simultaneously

present ethynyl and hydroxyl groups for reaction with azides and activated carboxylic acids (**2c**, Fig. 2H), (iii) nanofibers without functional groups (**2d**, Fig. 2I) as a non-reactive reference, (iv) polycationic pyridine-functionalized nanofibers (**2e**, fig. S9), and (v) water-repelling perfluoro-functionalized nanofibers (**2f**, fig. S9). Additionally, we used CVP into LCs to generate polymeric nanofibers with distinct main chains, including (vi) biodegradable polyester nanofibers (**2g**, ROP process, fig. S9) and (vii) semiconducting poly(phenylene vinylene) nanofibers (**2h**, Gilch process, fig. S9). When templated by nematic TL205, nanofibers made of polymers **2b-2h** were morphologically similar (Fig. 2, G to I and fig. S9 A to D), and possessed infrared spectroscopic signatures of the constituent chemical groups (Fig. 2, J to L and fig. S9, E to H).

LC ordering within films is influenced by interactions with confining surfaces, LC elastic moduli, and molecular properties of LCs including chirality (*19*), thus offering access to a diverse range of LC templates for CVP. For example, a film of nematic 5CB prepared with planar and homeotropic anchoring at bottom and top LC surfaces, respectively, leads to a bent and splayed internal ordering of the LC that templates banana-shaped nanofibers (Fig. 3A). Smectic LCs, with a statistical layering of oriented molecules (*19*), templated straight nanofibers with broadened tips arranged in conical fan-like morphologies (Fig. 3B) (*24*). Chiral nematic phases (cholesteric) yielded shape-controlled and chiral nanofiber assemblies with micrometer-scale periodicities (11.5 ± 1.5 μm and 11.3 ± 1.5 μm for S- and R-templated nanofibers, respectively) and an organization consistent with the fingerprint pattern characteristic of cholesteric films (periodicity of 10.8 ± 1.2 μm and 10.7 ± 1.1 μm for S- and R-handed cholesteric phase, respectively; Fig. 3C and fig. S10). The chirality of the LC also influenced the handedness of the nanofibers, as confirmed by circular dichroism spectroscopy of surface-immobilized and solvent-dispersed nanofibers (figs. S11 and S12) (*25*). In contrast to all other LC phases, a three dimensional network of helical nanofibers was formed by CVP into blue phase LCs, reflecting nanofiber growth templated by a three-dimensional network of double-twisted LC and line defects (Fig. 3D) (*26*). Overall, these results reveal that the shape, interfacial orientations and morphologies of the nanofiber arrays are templated by the structure of the LC phase. The LC transition temperatures remain almost unaltered by CVP (fig. S13), consistent with our conclusion (fig. S14) that the monomer concentration in the templating LC phase during nanofiber formation is low. These findings differ from conventional polymerizations in LCs, where the dynamic interplay between the

polymerization process and the LC template phase behavior makes control of the resulting polymeric nanostructures difficult, and often leaves unreacted monomers in the sample (*26-28*).

Figure 4A-D shows that CVP into conformal films of nematic E7 formed over the outer or inner surfaces of a hollow cylinder yielded arrays of nanofibers (97.5 ± 17.5 nm in diameter) anchored on the curved surfaces of the cylinder. On the inner surface, the density of the nanofibers decreased with increasing distance from the open end (Fig. 4D). Mesoscopic nanofiber islands were templated from micrometer-sized LC droplets electro-sprayed onto surfaces, thus providing a scalable approach for fabrication of arrays (Fig. 4E-F). We found also that free-standing LC films formed within metallic meshes or at the ends of capillaries (Fig. 4G) templated organized nanofiber assemblies (Fig. 4, H and I). Additionally, microbeads dispersed in LC phases prior to CVP supported growth of nanofibers and co-polymerization was used to create nanofibers for co-immobilization of different biomolecules (fig. S15).

Overall, our results reveal that CVP into LC templates enables scalable fabrication of arrays of polymeric nanofibers with programmable shapes, chemistries and long-range lateral organization, yielding interfacial properties currently unavailable by other techniques. For example, we found that it was possible to manipulate nanofiber chirality to control adhesion between surfaces. As shown in Fig. 4J and K, we measured adhesion to be higher for surfaces decorated with nanofibers than the corresponding flat CVP films, with the relative chirality of the nanofibers presented by the two surfaces also influencing the magnitude and selectivity of adhesion (Fig. 4K). Other properties designed into nanofiber arrays prepared by LC-templated CVP include wettability, intrinsic photoluminescence, biodegradability, and surface charge (Fig. 4J-K and fig S16). We envisage that additional functional properties can be realized by exploiting the full diversity of LC templates (*17, 19*) along with other polymerization mechanisms using vapor phase delivery of monomers.

References and Notes:

1. A. J. Hudspeth, *Nat. Rev. Neurosci.* **15**, 600-614 (2014).
2. H. E. M. Liwanag, A. Berta, D. P. Costa, S. M. Budge, T. M. Williams, *Biol. J. Linnean Soc.* **107**, 774-787 (2012).
3. N. Hirokawa, *Science* **279**, 519-526 (1998).
4. W. Barthlott, C. Neinhuis, *Planta* **202**, 1-8 (1997).
5. K. Autumn *et al.*, *Nature* **405**, 681-685 (2000).
6. T. Svedberg, *Kolloid Z* **18**, 54-56 (1916).
7. A. Matsumoto, S. Nagahama, T. Odani, *J. Am. Chem. Soc.* **122**, 9109-9119 (2000).
8. X. Wang, D. S. Miller, E. Bukusoglu, J. J. de Pablo, N. L. Abbott, *Nat. Mater.* **15**, 106-112 (2016).
9. T. J. White, D. J. Broer, *Nat. Mater.* **14**, 1087-1098 (2015).
10. K. Akagi, *Chem. Rev.* **109**, 5354-5401 (2009).
11. F. Bally-Le Gall *et al.*, *Chem.-Eur. J.* **23**, 13342-13350 (2017).
12. X. P. Deng, J. Lahann, *J. Appl. Polym. Sci.* **131**, 40315 (2014).
13. W. F. Gorham, *J Polym Sci A1* **4**, 3027-3039 (1966).
14. K. M. Vaeth, K. F. Jensen, *Macromolecules* **31**, 6789-6793 (1998).
15. O. Schafer *et al.*, *Synthetic Met* **82**, 1-9 (1996).
16. F. Xie *et al.*, *Angew. Chem.-Int. Edit.* **56**, 203-207 (2017).
17. D. Demus, J. Goodby, G. W. Gray, H.-W. Spiess, V. Vill, *Handbook of Liquid Crystals*. (Wiley-VCH Verlag GmbH, New York, 1998), vol. 2
18. Y.-K. Kim, X. Wang, P. Mondkar, E. Bukusoglu, N. L. Abbott, *Nature* **557**, 539-544 (2018).
19. P. G. de Gennes, J. Prost, *The Physics of Liquid Crystals*. (Clarendon Press, Oxford, 1993).
20. N. Podoliak *et al.*, *RSC Adv.* **4**, 46068-46074 (2014).
21. W. Iglesias, N. L. Abbott, E. K. Mann, A. Jakli, *ACS Appl. Mater. Interfaces* **4**, 6883-6889 (2012).
22. A. Bogi, S. Faetti, *Liq. Crysts.* **28**, 729-739 (2001).
23. S. Faetti, M. Gatti, V. Palleschi, T. J. Sluckin, *Phys. Rev. Lett.* **55**, 1681-1684 (1985).
24. V. Designolle, S. Herminghaus, T. Pfohl, C. Bahr, *Langmuir* **22**, 363-368 (2006).
25. R. Kuroda, T. Honma, *Chirality* **12**, 269-277 (2000).
26. F. Castles *et al.*, *Nat. Mater.* **11**, 599-603 (2012).
27. M. Mizusaki, K. Nakai, S. Enomoto, Y. Hara, S. Yusa, *Polym J* **49**, 457-463 (2017).
28. Y. Nakanishi, K. Okamoto, *Jpn. J. Appl. Phys.* **51**, 041701 (2012).
29. B. H. Clare, O. Guzman, J. de Pablo, N. L. Abbott, *Langmuir* **22**, 7776-7782 (2006).
30. R. J. Carlton *et al.*, *Liq. Cryst. Rev.* **1**, 29-51 (2013).
31. D. B. Williams, C. B. Carter, *Transmission Electron Microscopy: A Textbook for Materials Science*. (Springer, 2009).

Acknowledgments:

We thank Y. Dong, C. Lu, S. Rahmani and B. Plummer for help with SEM and TEM, V. Subramanian and the University of Michigan Biophysics NMR center for help with the solid state NMR analysis, and N. Kotov for insightful comments on the manuscript. **Funding:** This study was supported by the Army Research Office (W911NF-11-1-0251 and W911NF-17-1-0575). We thank the Michigan Center for Materials Characterization and University of Wisconsin Materials

Research Science and Engineering Center (DMR-1720415). The experiments performed with blue phase liquid crystals at University of Wisconsin-Madison were supported by the Department of Energy (DE-SC0004025). J.L. and C.H. acknowledge support from the German Science Foundation (SFB 1176, Project B3) and F.X. acknowledges funding from the China Scholarship Council and Northwestern Polytechnical University, China. **Author contributions:** N.L.A. and J.L. proposed and supervised the project; K.C.K.C., M.A.B.-P., and Y.-K.K. conducted experiments with assistance from J.V.G., F.X., A.F., C. H., K. S.; K.C.K.C., M.A.B.-P., Y.-K.K., N.L.A., and J.L. analyzed the data and wrote the manuscript with input from all co-authors. **Competing interest:** The University of Wisconsin-Madison and University of Michigan have filed a patent application (PCT/US17/27764) on the work described in this manuscript. **Data and materials availability:** All data supporting the findings of this study are available in the paper are present in the manuscript or the supplementary material.

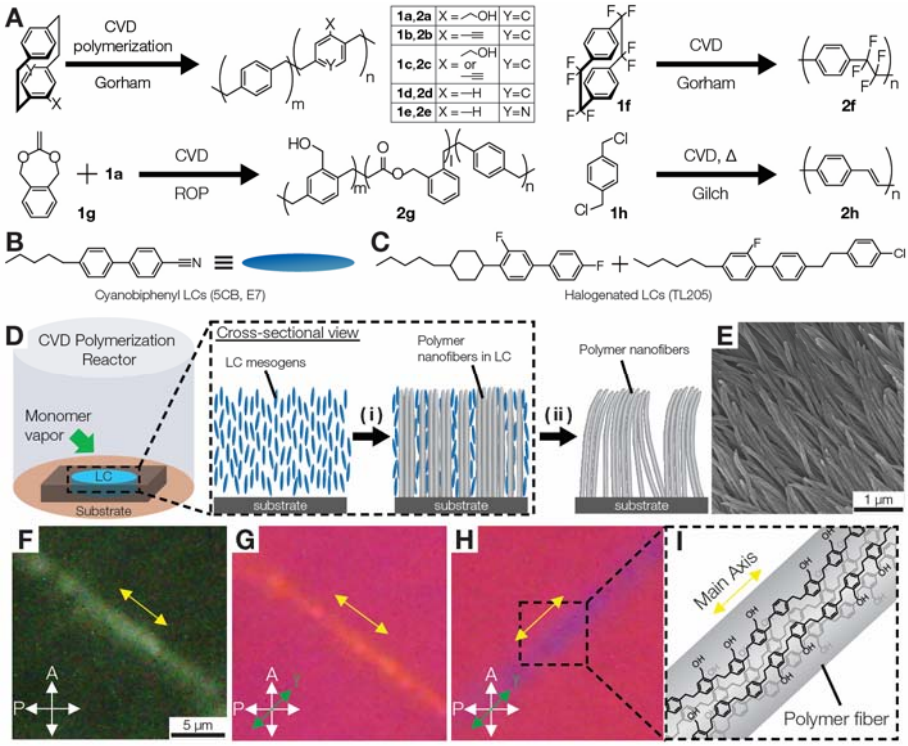

Fig. 1. Templated synthesis of nanofiber arrays via CVP into anisotropic media. (**A**) CVP of **1a-h** yields polymers **2a-h**. (**B**, **C**) Representative chemical structures of cyanobiphenyl-based (5CB and E7) and halogenated (TL205) LCs. (**D**) Fabrication of polymer nanofibers via CVP into a LC phase aligned perpendicular to the substrate. (**E**) SEM images of nanofibers polymerized from **1a** (10 mg) in 5CB. After the nanofiber synthesis, the LC template was removed. (**F**) Optical micrograph (crossed polars) of a nanofiber. Orientations of the analyzer (A) and polarizer (P) are shown in the double-arrow cross. (**G**, **H**) Micrographs (crossed polars) of the nanofiber with a quarter wave plate with its slow axis (γ, green double-arrow) (**G**) perpendicular or (**H**) parallel to the fiber axis; lower order interference colors (yellow) indicate a decrease in retardance. (**I**) Analysis of interference colors of the nanofiber in (**G**) and (**H**) indicates orientation of the polymer chains aligned along the fiber axis.

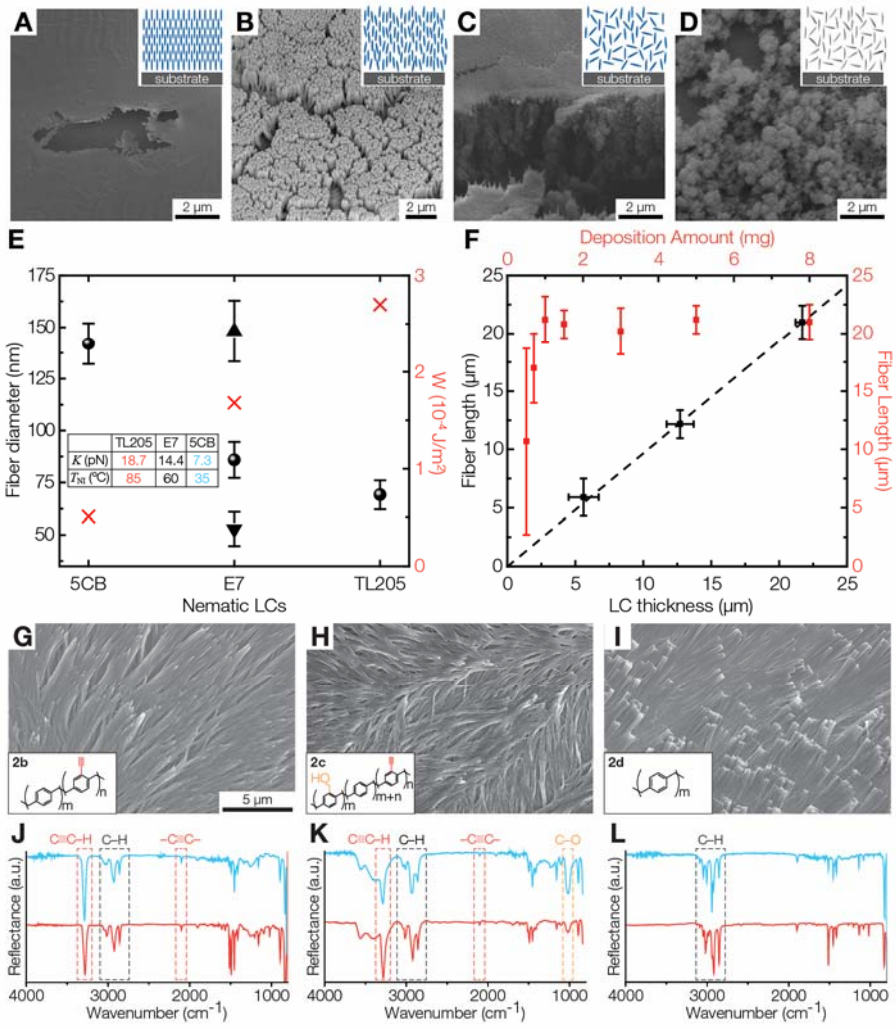

Fig. 2. Templated CVP of nanofibers with precise lengths, diameters and surface chemistries. (**A-D**) SEM images of nanofibers formed by CVP of **1a** (10 mg) with the indicated templates (see insert): (**A**) crystalline 5CB at 13 °C, (**B**) nematic 5CB at 25 °C, (**C**) isotropic 5CB at 37 °C, and (**D**) isotropic silicone oil at 25 °C. The LC thickness was 21.7 ± 0.5 μm. (**E**) Nanofiber diameters obtained by CVP of **1a** (6 mg) into E7 at 13 °C (down triangle), 25 °C (circles), 30 °C (up triangle), and 5CB, E7, and TL205 at 25 °C; the right axis shows the surface anchoring energy density W for each LC at 25 °C; the inset table shows elastic constants (K) at 25 °C and the nematic-isotropic phase transition temperatures (T_{NI}) of TL205, E7, and 5CB. (**F**) Nanofiber length as a function of either nematic E7 film thickness (black points) or mass of polymerized **1a** for a LC film with thickness of 21.7 ± 0.5 μm (red points). Mean ± SD, $N \geq 10$. (**G-L**) Representative (**G-I**) SEM images and (**J-L**) FTIR spectra of (**G**, **J**) **2b**, (**H**, **K**) **2c** and (**I**, **L**) **2d** templated into TL205. FTIR spectra of the nanofibers (red) are compared to polymer films synthesized without the LC phase (blue). LCs were removed prior to imaging and FTIR analysis.

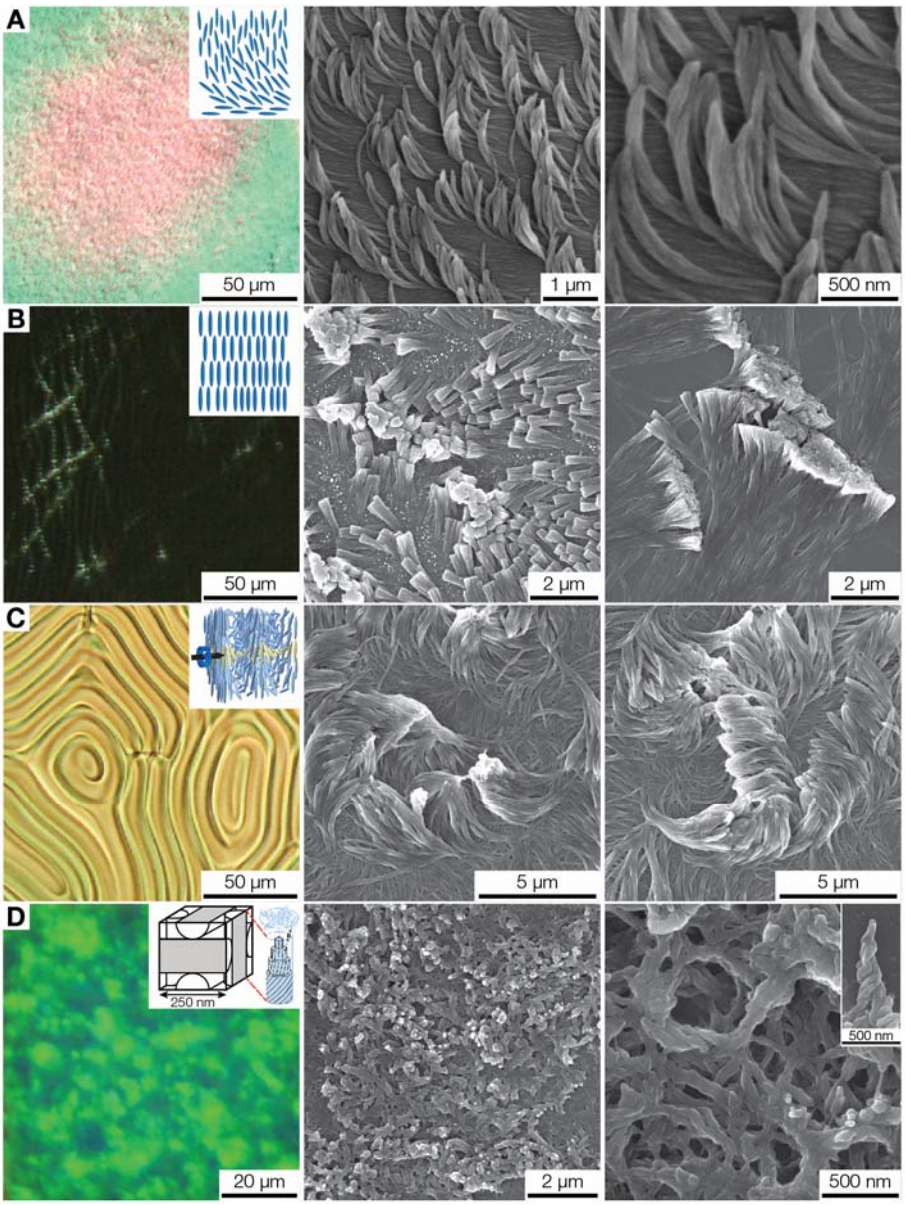

Fig. 3: Influence of LC template on nanofiber morphology and organization. (**A-D**) Left column: Optical micrographs (top view, crossed polars) of LC templates. Insets are schematic illustrations (side view) of molecular order within the LC templates; Right two columns: SEM images of nanofibers templated from the LCs. (**A**) Nematic film of E7 with hybrid anchoring and resulting banana-shaped nanofibers. (**B**) Homeotropically-oriented film of a Smectic A LC phase and the resulting polymeric nanostructures. (**C**) Micrograph showing cholesteric LC phase of E7 doped with a left-handed chiral dopant (S-811). SEM images in central and right columns show nanofibers templated from E7 containing left- (S-811) and right- (R-811) handed dopants, respectively. (**D**) Blue phase LC (BP1) with a cubic lattice spacing of ~250nm and the resulting polymeric nanostructure.

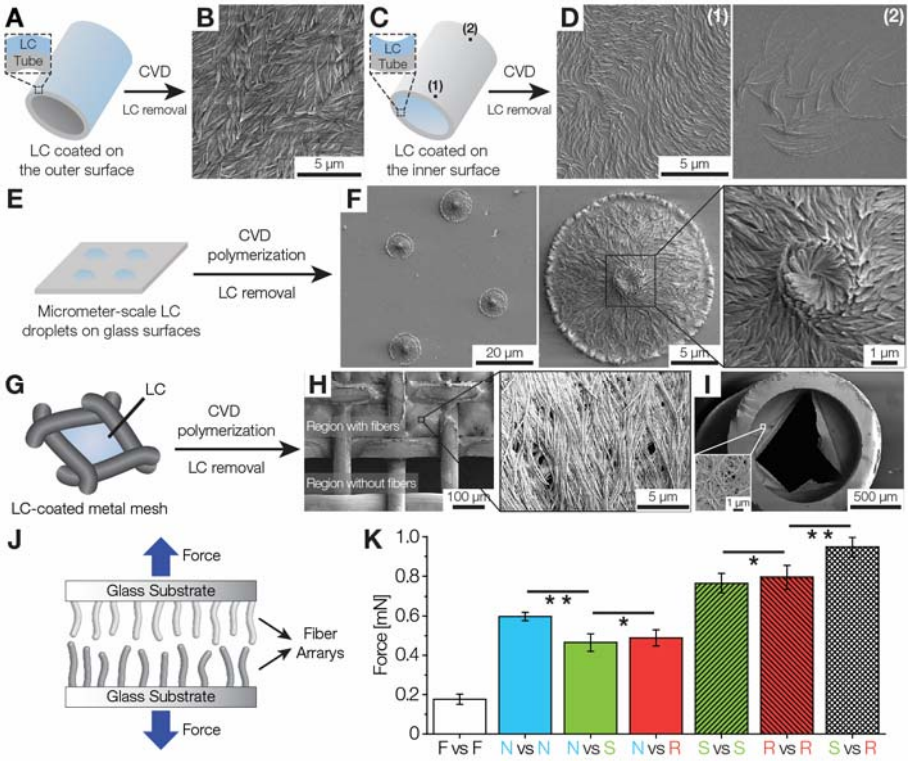

Fig. 4. Templated CVP of polymeric nanofibers in complex geometries. (**A-D**) CVP of **1a** into nematic E7 films coated on either (**A**) the exterior or (**C**) interior surfaces of glass capillaries and (**B**, **D**) SEM images of corresponding nanofibers ((1) indicates the region closest to the orifice). (**E**) CVP of **1a** into E7 microdroplets on a glass surface and (**F**) SEM images of the nanofiber assemblies. (**G**) CVP of **1a** into free standing films of E7 hosted within a stainless-steel mesh and (**H**) SEM image of suspended nanofiber film. (**I**) SEM image of nanofiber membrane spanning the tip of a glass capillary, which was initially intact, but was opened during microscopy revealing an ultrathin nanofiber array. (**J**) Schematic illustration of two substrates coated with nanofiber arrays prepared by CVP. (**K**) Adhesion forces between pairs of substrates decorated by flat CVP films (F) or nanofiber arrays templated from nematic (N), left-handed cholesteric (S) or right-handed cholesteric (R) LC phases. Mean ± SD, $N \geq 5$. Results marked with an asterisk (*) and double asterisks (**) are statistically identical ($p > 0.4$) and different ($p < 0.002$), respectively.

Supplementary Materials:

Materials and Methods

Figs. S1 to S16

References (*29-31*)